Physical Communication 47 (2021) 101401

Contents lists available at ScienceDirect

Physical Communication

journal homepage: www.elsevier.com/locate/phycom

Full length article

Feasibility study of 28 GHz and 38 GHz millimeter-wave technologies for fog radio access networks using multi-slope path loss model

Alaa Bani-Bakr [a], Kaharudin Dimyati [a,*], MHD Nour Hindia [a], Wei Ru Wong [a], Muhammad Ali Imran [b]

[a] Department of Electrical Engineering, Faculty of Engineering, Universiti Malaya, Kuala Lumpur, 50603, Malaysia
[b] School of Engineering, University of Glasgow, Glasgow, G12 8QQ, UK

ARTICLE INFO

Article history:
Received 28 May 2020
Received in revised form 8 April 2021
Accepted 12 June 2021
Available online 15 June 2021

Keywords:
Determinantal point process
Dual-slope path loss model
Fog computing
Ginibre point process
Ultra-dense network

ABSTRACT

Fog computing is considered a promising technology to reduce latency and network congestion. Meanwhile, Millimeter-wave (mmWave) communication owing to its potential for multi-gigabit of wireless channel capacity could be employed to further improve the performance of fog computing networks. In this context, we study the feasibility of using 28 GHz and 38 GHz mmWaves in fog radio access networks (F-RANs). The multi-slope path loss model is used to calculate the interference impacts because it provides a more accurate approximation of the wireless links. Simulations are carried out for uplink scenario considering the following fog node (FN) deployment models: Poisson point process (PPP), Ginibre point process (GPP), square grid, and ultra-dense network (UDN). The results depict that at low FN densities the massive accumulation of interference components severely impacts the performance. However, the performance can be improved by increasing the FN density and choosing a deployment strategy with high degree of regularity. Based on the results, we verify that it is feasible to use 28 GHz and 38 GHz mmWaves in F-RANs when the density of the interfering users is less than 150 user/km^2 where capacities higher than 1 Gbps are achieved for all considered scenarios.

1. Introduction

In the era of internet of things (IoT), the number of cellular IoT devices is anticipated to increase dramatically to reach unprecedented level in the next few years. Ericsson forecasts that by 2023 there will be around 3.5 billion cellular IoT connections [1]. This is mainly due to IoT capability to afford anything, anywhere and anytime interconnection and intercommunication, which paves its way to invade various applications such as smart homes and healthcare [2–5], in such way that IoT became an indispensable enabling technology for the aforementioned applications. The previously mentioned plethora in IoT applications and the number of its related interconnected things (i.e. smart devices) is accompanied with a proliferation in the amount and type of data generated by "things". Traditionally, cloud computing was considered as an efficient enabling technology to process IoT data, chiefly due to its mega computation and storage capabilities [6]. However, as the IoT data is predicted to grow exponentially the available bandwidth cannot afford a constant connection among "things" and the cloud, and the clouds themselves would be bottlenecked [7–9]. Moreover, many IoT applications such as healthcare applications are delay sensitive where very quick responses based on real-time analysis are required, meanwhile the high communication latency is a key limitation of cloud computing [10], owing to the fact that cloud computing is a centralized paradigm in which the data generated by the IoT devices needs to be sent to a centralized cloud data center in order to perform processing, computation and storing it.

To tackle these issues, Fog computing was proposed by Cisco in 2012 as a novel distributive computing paradigm that places the cloud computing resources including computation, networking, and storage in a hierarchical layered architecture between the cloud computing data centers and the "things" [11–14]. In fog computing, the fog node (FN) (i.e. edge node) has some processing, computation and storage capabilities, which enables it to perform processing of the latency sensitive IoT data, whereas the latency tolerant data and the data that require intensive computation can be forwarded to be processed in the cloud data center [15].

Meanwhile, as the world is witnessing the dawn of fifth-generation (5G), it is noteworthy to address that the 5G developers early vision was to improve the 5G communication networks performance as compared with the fourth generation (4G) in

* Corresponding author.
E-mail addresses: alaa.1710@siswa.um.edu.my (A. Bani-Bakr), kaharudin@um.edu.my (K. Dimyati), nourhindia@um.edu.my (M.N. Hindia), weiru@um.edu.my (W.R. Wong), Muhammad.Imran@glasgow.ac.uk (M.A. Imran).

https://doi.org/10.1016/j.phycom.2021.101401
1874-4907/

order to achieve the following performance indicators: 1000-fold higher mobile data volume per geographical area, 100-fold higher data rate per user, 100-fold expansion in the number of connected devices and 5-fold reduction in the end-to-end delay [16]. The former objectives can be achieved by adopting fog computing as an enabler. Though, the key viable enabling technique to increase the data rates is to exploit the large amount of vacant raw bandwidth in the mmWave bands [17]. Recently, 28 GHz and 38 GHz mmWave bands have been standardized by 3rd Generation Partnership Project (3GPP) under the 5G New Radio (NR) FR2 band guidelines (i.e. 3GPP Release 16) [18], also the bands have been allocated by the United States (US) Federal Communications Commission (FCC) for 5G networks under the new Upper Microwave Flexible Use License (UMFUS) designation [19]. Moreover, 28 GHz and 38 GHz mmWave bands are dedicated for 5G in China [20]. Thus, it is anticipated that 28 GHz and 38 GHz mmWave bands will play a key role in 5G deployments and Beyond-5G systems. However, utilizing the mmWaves in wireless communication systems has some limitations such as the mmWaves wireless propagated signals are susceptible to blockages by obstacles, shadowing, refraction, diffraction and they experience a higher path loss. Moreover, they are vulnerable to atmospheric absorption and rain attenuation [17,21,22]. This is mainly raising from their extremely short wavelengths in terms of (1 mm–10 mm), which are smaller than the physical dimensions of the obstacles in the surrounding environment.

Consequently, prior to design a mmWaves communications system, it is essential to gain a better understanding of mmWaves propagation behavior in order to optimally exploit the substantial advances of high date rates and enhanced capacity of mmWaves signals. Commonly, this can be achieved by characterizing the wireless propagation channel by modeling the path loss [22], owing to the fact that it is a measure of the propagated signal fading as a function of the signal frequency and the propagation distance. Traditionally, single-slope models are adopted to characterize the mmWave channels. This is mainly due to their simplicity as the path loss is expressed by a simple mathematical formula, wherein only a one single-slope line is used to characterize path loss over the propagation distance range. However, Multi-slope models have shown higher accuracy in modeling the mmWaves propagation loss, which is due to characterizing the path loss using different slopes for different regions of the wireless link [23–27]. Therefore, using the multi-slope models in the mmWaves communication system studies is drawing more attention recently.

Relishing the potentials of the extremely low latency and the high data rates can be achieved by integrating both mmWave wireless communication networks and fog computing paradigm. In such mmWave IoT F-RANs, the communication between the edge devices (i.e. "things") and the FNs is performed by using a mmWave frequency carrier, while the FNs perform the required processing and computation on the received data from the edge devices, and forward the unprocessed data to the core cloud center via a mmWave wireless link or a wireline Ethernet link. In this hyperconnected IoT F-RAN architecture, a high interference generation is anticipated due to the simultaneous massive uplink data transmission from the densely deployed edge devices to their associated FNs. Moreover, since 28 GHz and 38 GHz mmWave frequencies are candidate frequency bands to be used in 5G and Beyond-5G systems. Thus, this paper proposes a simulation-based feasibility study of using 28 GHz and 38 GHz mmWave frequencies in hyperconnected F-RANs. Taking into consideration the interference components generated by the simultaneous uplink transmissions of deployed edge devices, the proposed study utilizes Shannon's formula to calculate the channel capacity of one main mmWave uplink transmission between a typical edge device and its associated FN. For a more precise feasibility study using 28 GHz and 38 GHz mmWave frequencies in F-RANs, we employ multi-slope path loss models, also the main lobe profile of the steerable antenna radiation pattern is formulated using a Gaussian function. As far as the authors know, no study before estimated the performance of F-RANs using multi-slope models. Our main contributions can be summarized as follows:

- The achievable channel capacity of uplink 28 GHz and 38 GHz mmWave F-RANs is evaluated under dual-slope, line-of-sight (LOS) and non-line-of-sight (NLOS) single-slope models, where Poisson Point Process (PPP), Ginibre point process (GPP), and square grid models are used to model the FN network. We show that the FN network models with higher degree of regularity perform better. We also show that mmWave F-RANs using 28 GHz and 38 GHz frequencies can achieve capacities of multi-gigabit.
- The interference impacts are analyzed and we show that the massive accumulation of the interference components can severely degrade the channel capacity to drop below 1 Gbps levels when the density of the interfering edge users increases beyond 150 interfering user/km^2.
- The impacts of the network densification are also studied, where the simulation results show that increasing the FN density improves the network performance, and this improvement is obvious in ultra-dense network (UDN) deployment model, where capacities higher than 3 Gbps are achieved even at high densities of interfering edge devices.

The rest of the paper is organized as follows. Section 2 discusses the relevant work. The system model and the FN deployment strategies are presented in Section 3. Section 4 introduces the 28 GHz and 38 GHz mmWaves propagation models and characteristics. The details of estimating the capacity using Shannon's formula are described in Section 5. In Section 6, we present the results and discussions. The limitations and future research directions are delivered in Section 7. Finally, the concluding remarks are given in Section 8.

2. Related work

The key gain realized when utilizing directional mmWave system i.e. through antenna beamforming is the capacity improvement. In these systems the interference probability depends mainly on the antenna radiation pattern which can be calculated by

$$Pr(interference) = \frac{\varphi_{hp}}{360^\circ} \cdot \frac{\vartheta_{hp}}{180^\circ} \quad (1)$$

where φ_{hp} ($0^\circ \leq \varphi_{hp} \leq 360^\circ$) is the 3 dB half-power beamwidth in azimuth plane and ϑ_{hp} ($0^\circ \leq \vartheta_{hp} \leq 180^\circ$) is the 3 dB half-power beamwidth in elevation plane [28]. Hence, as the beamwidth in the directional mmWave wireless systems is conventionally assumed to be narrow in the range of 1° to 10° the interference probability will be very small and the interference impact is usually assumed to be ignorable.

However, intensive numerical simulations of highly directional mmWave systems in [29,30] have shown that the interference impact may not be ignorable when the number of interfering paths is large. In [29], 60 GHz mmWave propagation and the impacts of interference on the main uplink channel of a cloud-enabled visual data uploading wireless networks were studied and simulated. The theoretical study in [29] was performed using a Gaussian mainlobe profile for the steerable antenna radiation patterns and 60 GHz LOS path loss model of IEEE 802.11ad. Whereas the work in [30] used the same path loss model but

with the standardized antenna radiation patterns of International Telecommunication Union (ITU) to study the interference impacts to a 60 GHz mmWave wireless propagation in hyperconnected F-RANs. However, our work is different from the work in [29,30] not only because both studies consider 60 GHz mmWave radio propagation whereas this paper studies 28 GHz and 38 GHz mmWave bands, but also because our work uses the multi-slope path loss models, which is more accurately characterize the mmWave radio propagation by more closely capturing the path loss dependency on the propagated distance. Moreover, the access points deployment in [29,30] is deterministic, i.e. the locations of the FNs are predetermined such that FNs form a rectangular shape network consisting of 8 FNs, wherein the impacts of the location of deployed FNs network and number of interfering users on the channel capacity were investigated. Whereas in this paper, both stochastic and deterministic models are used to model the spatial locations of the FNs. In specific, this paper considers PPP and GPP stochastic models to model the spatial locations of the FNs to study the impacts of the complete randomness and the repulsion between the FNs on the performance, respectively. Also, this paper considers the deterministic square grid FN deployment model, in which the FNs are regularly deployed, and the UDN deployment model, wherein the impact of the FNs ultra-densification on the channel capacity is investigated.

The achievable capacity using Shannon's formula of 38 GHz mmWave frequency band was investigated in [31], wherein the interference impacts on the main-cells wireless downlink video streaming quality originating from wireless transmissions of small-cells have been simulated and analyzed using single-slope Close-In path loss model and the standardized antenna radiation patterns of ITU. Whereas this paper provides a deeper and more accurate study of 38 GHz mmWave communication systems by taking into account the multi-slope characterization of the path loss and the random deployment of the access points.

3. System model

We consider the hyperconnected IoT F-RAN system illustrated in Fig. 1, which consists of a set IoT edge devices designated as IoT user equipment UE $= \{UE_1, UE_2, \ldots, UE_n\}$. The gathered data by the UEs need to be offloaded via the mmWave uplink wireless access channel to the FNs to be processed. However, the FNs have a limited storage and computing capability. Thus, only the latency sensitive computation tasks will be executed at the FNs, while the other computation tasks will be forwarded to the central cloud where the computation tasks will be executed.

Due to the hyperconnected architecture of the F-RAN system, mmWave uplink transmissions between UEs and its associated FN suffer from the interference originating from other UEs reusing the same mmWave channel. Fig. 1 demonstrates two examples of the interference scenarios in the system, where the uplink mmWave transmission from UE_i to its associated access node FN_1 is experiencing interference originating from the wireless transmission of UE_j and UE_k to their associated access nodes FN_1 and FN_2, respectively. Due to the hyperconnected nature of the system the number of simultaneous uplink transmissions is anticipated to be high. Hence, in order to monitor the interference impacts in the matter of capacity reduction the accumulated interference should be considered. This numerical simulation study is to investigate the actual performance degradation in terms of the capacity reduction owing to the accumulated interference in such systems. In the following subsection we discuss the network deployment models considered in this study.

3.1. Network deployment models

We consider an uplink mmWave transmission scheme in which the wireless user equipment (UEs) are spatially distributed in the Euclidean plane $\mathbb{R}^2$ according to a homogeneous PPP Φ_u with density λ_u. We also consider a location based association scheme wherein each UE is connected with the closest FN to its location. With no loss of generality, we assumed that a typical UE resides at the origin. Whereas, for the FN deployment the following models are considered:

(a) **PPP model**: Homogeneous PPP is a spatial point process in which the number of points in a bounded region $\boldsymbol{b} \subset \mathbb{R}^2$ has a Poisson distribution (i.e. $Pr(N(\boldsymbol{b}) = n) = \frac{\lambda^n}{n!}e^{-\lambda}$, where λ is the spacial point density). PPP has the property of complete independence [32]. In other words, each point is stochastically independent of the others, and thus the point process is completely random. PPP is widely used in the literature to model locations of the access points due to its high analytical tractability [33,34]. However, PPP has the weakness of the access points are located very close together in some cases owing to the complete independence property [35], whereas in practical networks a repulsion (i.e. correlation) among the locations of the access points may exist. In the PPP model considered by this paper, the FNs' locations in a circular area in $\mathbb{R}^2$ are modeled as a homogeneous PPP Φ_{FN} with density λ_{FN}. Fig. 2a shows a realization of a PPP FNs' deployment over a circular disk of radius $r = 500$ m with density of $\lambda_{\text{FN}} = 40$ FNs/km^2.

(b) **GPP model**: In order to address the dynamic repulsion among the locations of the FNs to increase the coverage in practical networks, we consider GPP to model the spacial location of the FNs. The GPPs are a type of the determinantal point processes (DPPs), which form a class of repulsive point processes on the complex plane $\mathbb{C} = \mathbb{R}^2$. The probability distribution of the DPP is characterized as a determinant of some function. Accordingly, DPP and GPP are defined as follows:

Definition 1 (*DPP*)**.** Let Φ denote simple locally finite spatial point process on $\mathbb{R}^d$, and $\zeta^{(m)}$ denotes its nth correlation functions (joint densities) w.r.t. some Radon measure γ on $\mathbb{R}^d$; that is, for any Borel function B on $\mathbb{R}^{d\times n}$ with compact support,

$$E\left[\sum_{\substack{Z_1,Z_2,\ldots,Z_n\in\Phi\\ Z_i\neq Z_j, i\neq j}} B(Z_1, Z_2, \ldots, Z_n)\right] = \iint\cdots\int_{\mathbb{R}^{d\times n}} B(z_1, z_2, \ldots, z_n)\zeta^{(n)}(z_1, z_2, \ldots, z_n)\prod_{i=1}^{n}\gamma(dz_i) \tag{2}$$

where E stands for the expectation w.r.t. the distribution of Φ, and $\zeta^{(n)}(z_1, z_2, \ldots, z_n) \times \prod_{i=1}^{n}\gamma(dz_i)$ is the probability of finding a point in the vicinity of each $z_i, i = 1, 2, \ldots, n$. The point process Φ is stated to be a DPP on $\mathbb{R}^d$ with kernel $\mathcal{K} : \mathbb{R}^d \times \mathbb{R}^d \to \mathbb{C}$ w.r.t. locally finite reference measure γ if $\zeta^{(n)}$ satisfy $\zeta^{(n)}(z_1, z_2, \ldots, z_n) = det[\mathcal{K}(z_i, z_j)_{i,j=1,2,\ldots,n}]$, where $det[\mathcal{K}(z_i, z_j)_{i,j=1,2,\ldots,n}]$ accounts for the determinant of the $n\times n$ matrix with (i, j)th entry $\mathcal{K}(z_i, z_j)$ [36].

Remark 1. In order to ascertain the existence of DPP Φ, the following assumptions should be taken:The kernel $\mathcal{K}$ is a continuous complex covariance function on $\mathbb{R}^d \times \mathbb{R}^d$, i.e. $\mathcal{K}$ is positive semidefinite and Hermitian such that $\mathcal{K}(z, w) = \overline{\mathcal{K}(z, w)}$ for $z, w \in \mathbb{R}^d$, where $\overline{\mathcal{K}}$ is the complex conjugate of $\mathcal{K}$.

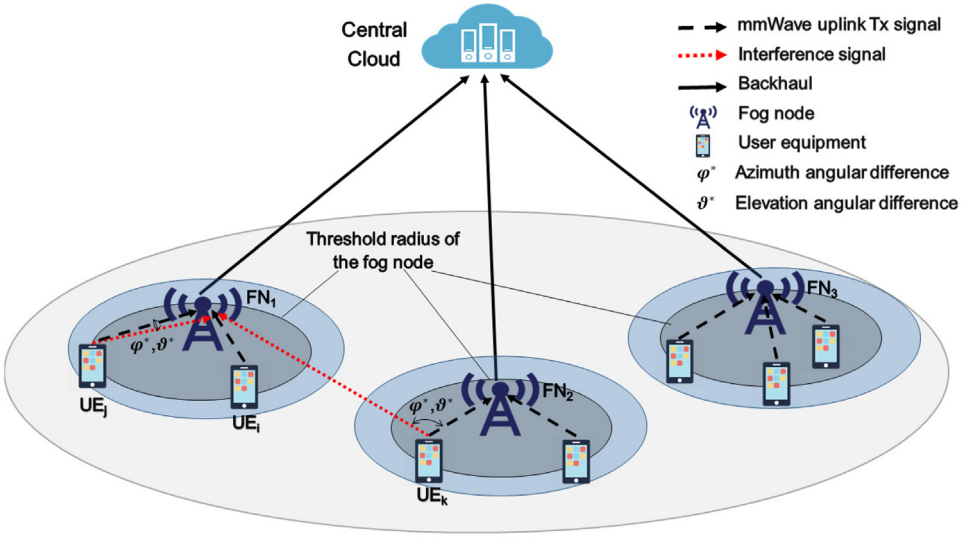

Fig. 1. Illustration of mmWave hyperconnected F-RAN system model.

Remark 2. A PPP is the special case of DPPs where $\mathcal{K}(z, w) = 0$ whenever $z \neq w$.

Remark 3. The spatial point density function of the DPP Φ w.r.t. the reference measure γ is

$$\zeta^{(1)}(z) = \mathcal{K}(z, z), \qquad z \in \mathbb{R}^d \tag{3}$$

and the expected number of points in Φ is given by the trace

$$\eta = E[\Phi] = \int \mathcal{K}(z, z)\gamma(dz) \tag{4}$$

Moreover, the pair correlation function is given by

$$R(z, w) = \begin{cases} \frac{\zeta^{(2)}(z,w)}{\zeta^{(1)}(z)\zeta^{(1)}(w)}, & \zeta^{(1)}(z), \zeta^{(1)}(w) > 0 \\ 0, & otherwise \end{cases} \tag{5}$$

Remark 4. The repulsiveness of DPPs can be reflected by the following facts. If $\mathcal{K}$ is continuous, then for $i \neq j$ we have $\zeta^{(n)}(z_1, z_2, \ldots, z_n) \to 0$ as $|z_i - z_j| \to 0$, and if $\mathcal{K}$ is Hermitian, then $R(z, w) \leq 1$ and for any $n = 2, 3, \ldots$

$$\zeta^{(n)}(z_1, z_2, \ldots, z_n) \leq \zeta^{(1)}(z_1)\zeta^{(1)}(z_2)\cdots\zeta^{(1)}(z_n) \tag{6}$$

with equality only if Φ is a PPP [37].

Definition 2 (*The Standard GPP*)**.** A DPP Φ on $\mathbb{C} \approx \mathbb{R}^2$ is called GPP if its kernel on $\mathbb{C} \times \mathbb{C}$ is given by

$$\mathcal{K}(z, w) = e^{z\overline{w}}, \qquad z, w \in \mathbb{C} \tag{7}$$

w.r.t. the Gaussian measure

$$\gamma(dz) = \frac{e^{-|z|^2}}{\pi}\upsilon(dz) \tag{8}$$

where υ stands for the Lebesgue measure on $\mathbb{C}$. The definition of the GPP by the pair $\mathcal{K}$ and γ is not distinct since Φ can be also obtained by considering the kernel $\widetilde{\mathcal{K}}(z, w) = \pi^{-1}e^{z\overline{w}-\left(|z|^2+|w|^2\right)/2}$ w.r.t. the Lebesgue measure $\widetilde{\gamma}(dz) = \upsilon(dz)$ [38].

The repulsiveness of GPPs can be proven be considering the pair correlation function. By definition, the GPP has a first-order density $\widetilde{\zeta}^{(1)}$ of π^{-1} w.r.t. the Lebesgue measure, whereas the second-order density of Φ is

$$\widetilde{\zeta}^{(2)}(z, w) = det\begin{bmatrix} \frac{1}{\pi}e^{z\bar{z}-\frac{|z|^2+|z|^2}{2}} & \frac{1}{\pi}e^{z\overline{w}-\frac{|z|^2+|w|^2}{2}} \\ \frac{1}{\pi}e^{\bar{z}w-\frac{|z|^2+|w|^2}{2}} & \frac{1}{\pi}e^{w\overline{w}-\frac{|w|^2+|w|^2}{2}} \end{bmatrix} = \frac{1}{\pi^2}\left(1 - e^{-\rho^2}\right) \tag{9}$$

where $\rho = |z - w|$. It follows that

$$R(z, w) = R(\rho) = \frac{\zeta^{(2)}(z, w)}{\zeta^{(1)}(z)\zeta^{(1)}(w)} = 1 - e^{-\rho^2} \tag{10}$$

then $R(\rho) \leq 1, \forall\rho$. Hence, GPP is exhibiting repulsiveness at all distances.

Definition 3 (*The Scaled GPP*)**.** Let $s > 0$ denote the scaling parameter which controls the spatial density of the point process. Then the scaled GPP Φ_s is a defined by a kernel of

$$\mathcal{K}(z, w) = e^{sz\overline{w}} \tag{11}$$

w.r.t. the reference measure

$$\gamma(dz) = \frac{s}{\pi}e^{-s|z|^2}\upsilon(dz) \tag{12}$$

the scaled GPP Φ_s can be also defined by considering the kernel $\widetilde{\mathcal{K}}(z, w) = s\pi^{-1}e^{s\left(z\overline{w}-\left(|z|^2+|w|^2\right)/2\right)}$ w.r.t. the Lebesgue measure $\widetilde{\gamma}(dz) = \upsilon(dz)$. The spatial density of Φ_s is equal to $s\pi^{-1}$ [33].

Fig. 2b depicts a realization of scaled GPP FN deployment with density of $\lambda_{FN} = 40$ FNs/km^2 over a circular disk of radius $r = 500$ m. Note that the GPP deployment of FN exhibits a higher degree of regularity compared to the PPP model in Fig. 2a.

(c) **Square grid model**: Square grid is a regular deployment of the access points which is considered a good approximation for Manhattan-like urban environments [39]. The grid-based deployment of the nodes is utilized in many applications such as traffic monitoring, power grid smart metering, goods monitoring in warehouses, and smart homes [40]. Moreover, as the square grid provides the ideal highest coverage, it is usually used as benchmark in wireless networks performance studies [41]. In the square grid model adopted by this work, the FNs are regularly placed at the centers of a square tessellation of side $2r/\lceil\sqrt{4\lambda_{FN}r^2}\rceil$ as shown in Fig. 2c, where $\lceil x\rceil$ denotes the largest

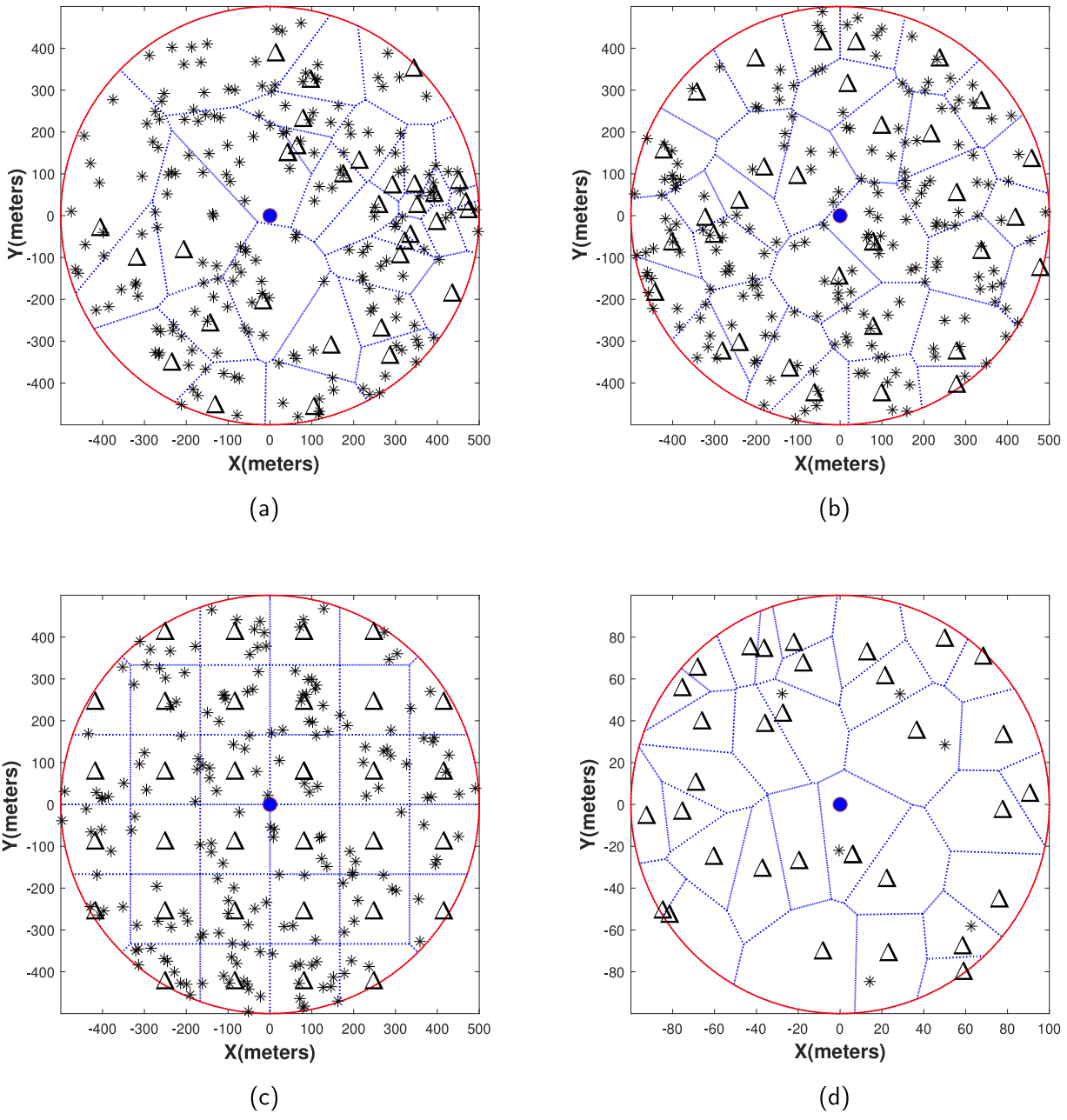

Fig. 2. Network deployment scenarios on a circular disk enclosed by solid line, UEs are marked with asterisk and deployed according to PPP with density of $\lambda_u = 250$ UEs/km^2, the circle marks a typical UE located at the origin, and the FNs are marked with triangle. The dotted lines are the edges of Voronoi tessellation. (a) PPP realization of FNs ($\lambda_{FN} = 40$ FNs/km^2), (b) GPP realization of FNs ($\lambda_{FN} = 40$ FNs/km^2), (c) Square grid realization of FNs ($\lambda_{FN} = 40$ FNs/km^2), (d) UDN scenario ($\lambda_{FN} = 10^3$ FNs/km^2).

integer number smaller than x, λ_{FN} is FN density and r is the radius of the deployment circular disk in the Euclidean plane $\mathbb{R}^2$.

(d) **UDN model**: mmWave UDN is considered an essential technology for 5G and beyond communication systems [42]. In UDN's, the increasing demands for higher data rates by the end users is satisfied by bringing the access points closer to the end users via the ultra-dense deployment of low power access points with small coverage area. According to [43], UDN's are defined as those networks in which the density of the access points (i.e. FNs) is much larger than the density of active users $\lambda_{FN} \gg \lambda_u$, in such way that $\lambda_{FN} \geq 10^3$ FNs/km^2, while $\lambda_u \leq 600$ active users/km^2. Recently, Haenggi has suggested to classify dense networks according to the devices density level using the same terminology used for frequency bands as shown in Table 1 [44]. However, the suggested classification does not take into consideration the density of the deployed access points, which is an important parameter. Therefore, this paper adopts [43] definition of UDN as it considers both the UE and FN densities, which can be viewed as 'below VHD UEs/ above UHD FNs' using the aforementioned classification. In this paper, we consider PPP Φ_{FN} to model the dense deployment of the FNs with density λ_{FN} that corresponds with the constraints of UDN definition of [43]. In Fig. 2d an example of an UDN over a circular area of radius $r = 100$ m is presented, where the FNs and UEs are modeled as PPP with $\lambda_{FN} = 10^3$ FNs/km^2 and $\lambda_u = 250$ UEs/km^2.

Note that in temporal systems, the time is divided into time slots, wherein each UE attempts to transmits its packet with

Table 1
Density classification.

	Density (/km^2)
High Dense (HD)	1–10
Very High Dense (VHD)	10–10^2
Ultra High Dense (UHD)	10^2–20^3
Super High Dense (SHD)	10^3–20^4
Extremely High Dense (EHD)	10^4–20^5
Tremendously High Dense (THD)	10^5–20^6

probability of p in each time slot [45]. Thus, the results obtained in this paper can be extended to take into account the temporal variation of the UEs by considering the point process of the active interfering UEs in each time slot, which is a thinned PPP with density $p\lambda_u$.

4. mmWave propagation characteristics

This section elaborates the fundamental characteristics of 28 GHz and 38 GHz mmWave radio propagation. The mmWaves path loss models are presented in Section 4.1, the oxygen attenuation is in Section 4.2, finally the steerable antenna radiation patterns are introduced in Section 4.3.

4.1. Path loss models

In this section, different models that characterize the large scale fading of mmWaves propagated signals are presented. Assuming no blockage between FNs and user devices, the Close-In single-slope model is given as:

$$PL_s(d) = \alpha + 10\beta \log_{10}(d) \tag{13}$$

where $PL_s(d)$ is the path loss in dB as a function of d which is the 3D separation distance between the transmitter and the receiver terminals in meters, β denotes the path loss exponent (PLE), and α represents the free space path loss in dB for a carrier wavelength λ_c:

$$\alpha = 20 \log_{10}\left(\frac{4\pi}{\lambda_c}\right) \tag{14}$$

Employing single-slope model in mmWave and UDN studies leads to lacking in accuracy, because it fails to precisely capture the PLE dependency on the physical environment in these networks. Thus, the dual-slope model has been proposed to overcome these limitations. The dual-slope model at a distance d can be expressed as [25,26,46]:

$$PL_d(d) = \begin{cases} l_1(d) = \alpha + 10\beta_1 \log_{10}(d), & d \le d_{th} \\ l_2(d) = l_1(d_{th}) + 10\beta_2 \log_{10}\left(\frac{d}{d_{th}}\right), & d > d_{th} \end{cases} \tag{15}$$

where d_{th} is the threshold distance in meters, α represents the free space path loss, β_1 stands for the PLE when the distance is smaller than d_{th}, and β_2 denotes the PLE when the separation distance is larger than d_{th}.

The dual-slope model can be extended into the N-slope model as [47]: Eq. (16) is given in Box I, where β_n, $n = \{1, 2, \ldots, N\}$ denotes the PLE suchlike $0 \le \beta_1 \le \beta_2 \le \cdots \le \beta_N$, and the threshold distance is represented by $d_{th}^{(n)}$, $n = \{1, 2, \ldots, N-1\}$ such that $d_{th}^{(1)} \le d_{th}^{(2)} \le \cdots \le d_{th}^{(N-1)}$.

4.2. Oxygen attenuation

For a more precise study of the mmWaves radio propagation behavior, we consider the oxygen attenuation (also known as atmospheric gases attenuation), which is given by

$$\Omega(d) = O_f \cdot \frac{d}{1000} \tag{17}$$

where d designates the propagated distance by the mmWaves radio signal and O_f denotes the oxygen attenuation factor, which depends on the carrier frequency and its values are about 0.11 dB/km and 0.13 dB/km for 28 GHz and 38 GHz mmWave, respectively [48].

4.3. Antenna radiation pattern

In this study, a two-dimensional Gaussian function is used to formulate the mainlobe of the reference steerable radiation pattern. The considered antenna gain of mmWave FNs and UEs using a Gaussian mainlobe profile is given as [29]:

$$G_{dBi}(\varphi, \vartheta) \approx G_0 - 12\left(\frac{\varphi}{\varphi_{hp}}\right)^2 - 12\left(\frac{\vartheta}{\vartheta_{hp}}\right)^2 \tag{18}$$

where G_0 stands for the maximum transmit antenna gain in dBi (assumed to be 24 dBi), φ ($-180° \le \varphi \le 180°$) is the azimuth angle, ϑ ($-90° \le \vartheta \le 90°$) denotes the elevation angle, and the values of the azimuth and elevation plane 3 dB half-power beamwidths are φ_{hp} and ϑ_{hp}, respectively. Moreover, φ_{hp} and ϑ_{hp} are interrelated as follows [49]:

$$\varphi_{hp} \cdot \vartheta_{hp} \approx 31 \times 10^{(3 - \frac{G_0}{10})} \tag{19}$$

assuming $\varphi_{hp} = \vartheta_{hp}$, their values can be calculated by:

$$\varphi_{hp} \approx \vartheta_{hp} \approx \left(31 \times 10^{(3 - \frac{G_0}{10})}\right)^{1/2} \tag{20}$$

The radiation patterns in azimuth and elevation planes of the considered reference steerable antenna at 24 dBi transmit antenna gain, can be plotted in as shown in Fig. 3.

5. Capacity calculations

The main wireless uplink (i.e. link i) for which the SINR and the channel capacity are calculated is the wireless mmWave uplink between the typical UE and its associated FN which is the closest FN to its location.

According to Shannon's formula, the wireless channel capacity at separation distance d between transmitter (i.e. the typical UE) and receiver (i.e. the FN connected with the typical UE) of the main link i can be calculated by

$$C_i(d) = BW \cdot \log_2\left(1 + \frac{S_{mW}^i(d)}{n_{mW} + I_{mW}^i}\right) \tag{21}$$

where BW is the channel bandwidth of the studied mmWave frequency (i.e. 1 GHz [50]), $S_{mW}^i(d)$ denotes the received signal power at the FN of main link i in milli-Watts (mW), I_{mW}^i is the accumulated interference in mWs to the main link i occurred by the wireless transmissions originating from the UE's in the system, and n_{mW} denotes the background noise in mWs. Note that, Shannon's capacity represents the maximum achievable data rate, which cannot be achieved in the latency sensitive data transmission scenario which requires short transmission delays [51].

A detailed explanation of $S_{mW}^i(d)$, I_{mW}^i and n_{mW} computation procedures are delivered in Sections 5.1 to 5.3.

5.1. Received signal calculations

The received signal strength in mWs at the FN of the main link i (i.e. $S_{mW}^i(d)$) can obtained by transforming the received signal power from dBm scale into mW scale as follows:

$$S_{mW}^i(d) = 10^{\left(\frac{S_{dBm}^i(d)}{10}\right)} \tag{22}$$

$$PL_m(d) = \begin{cases} l_1(d) = \alpha + 10\beta_1 \log_{10}(d), & d \le d_{th}^{(1)} \\ l_2(d_{th}^{(1)}, d) = l_1(d_{th}^{(1)}) + 10\beta_2 \log_{10}\left(\frac{d}{d_{th}^{(1)}}\right), & d_{th}^{(1)} < d \le d_{th}^{(2)} \\ l_3(d_{th}^{(1)}, d_{th}^{(2)}, d) = l_2(d_{th}^{(1)}, d_{th}^{(2)}) + 10\beta_3 \log_{10}\left(\frac{d}{d_{th}^{(2)}}\right), & d_{th}^{(2)} < d \le d_{th}^{(3)} \\ \vdots & \\ l_N(d_{th}^{(1)}, d_{th}^{(2)}, \ldots, d_{th}^{(N-1)}, d) = l_{N-1}(d_{th}^{(1)}, d_{th}^{(2)}, \ldots, d_{th}^{(N-1)}) + 10\beta_N \log_{10}\left(\frac{d}{d_{th}^{(N-1)}}\right), & d > d_{th}^{(N-1)} \end{cases} \quad (16)$$

Box I.

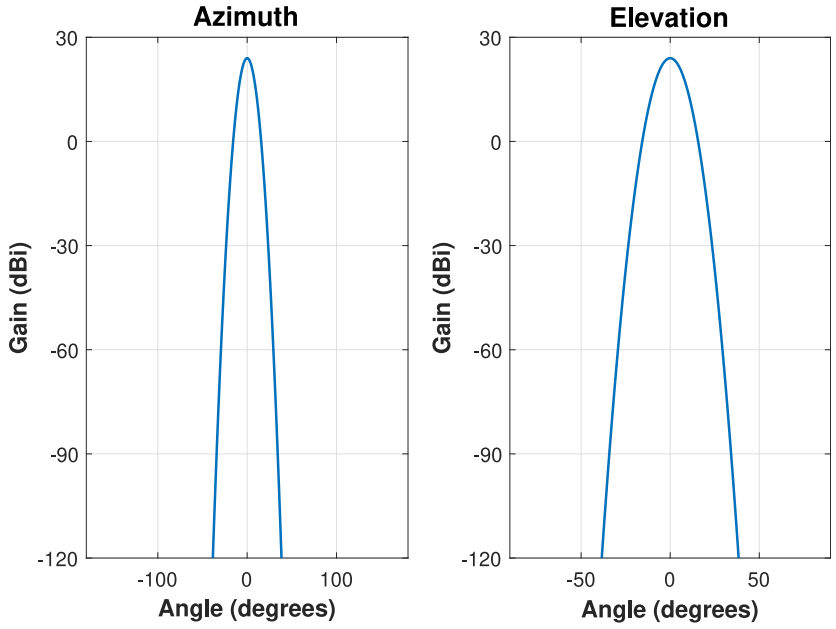

Fig. 3. The radiation patterns of the considered reference steerable antenna at 24 dBi transmit antenna gain.

where $S_{dBm}^{i}(d)$ stands for the received signal power in dBms at the FN of the wireless link i, which can be calculated as:

$$S_{dBm}^{i}(d) = P_{dBm}^{i} + G_{dBi}^{i,Tx}(\varphi^{\dagger}, \vartheta^{\dagger}) + G_{dBi}^{i,Rx} - \mathcal{L}(d) \quad (23)$$

where $P_{dBm}^{i}(d)$ is the transmit power of the typical UE, $G_{dBi}^{i,Tx}(\varphi^{\dagger}, \vartheta^{\dagger})$ is the transmit antenna gain of the typical UE, and $G_{dBi}^{i,Rx}$ is the receive antenna gain of the FN associated with the typical UE. In addition, $\mathcal{L}(d)$ represents the wireless channel attenuation as a function of the length of the main link i (i.e. d), which is given by:

$$\mathcal{L}(d) = PL(d) + \Omega(d) \quad (24)$$

where $PL(d)$ denotes the path loss and $\Omega(d)$ is the oxygen attenuation both are in dB scale.

In this paper we assumed that the receive antennas are omni-directional, thus ($G_{dBi}^{i,Rx} = 0$). Moreover, we assumed that the typical UE and the FN of the main link i are perfectly aligned. Thus, the radiation pattern azimuth angular difference $\varphi^{\dagger}$ and elevation angular difference $\vartheta^{\dagger}$ of the main link are set to zero (i.e. $\varphi^{\dagger} = \vartheta^{\dagger} = 0$). Also, we assumed that $G_{dBi}^{i,Tx}(\varphi^{\dagger}, \vartheta^{\dagger}) =$ 24 dBi and $P_{dBm}^{i} = 19$ dBm such that the equivalent isotropically radiated power (EIRP) (i.e. $EIRP = G_{dBi}^{i,Tx}(\varphi^{\dagger}, \vartheta^{\dagger}) + P_{dBm}^{i}$) coincide with its limit of 43 dBm in USA.

5.2. Interference calculations

In the previously stated Shannon's formula the accumulated interference can be calculated as:

$$I_{mW}^{i} = \sum_{j \in \mathcal{J}, j \neq i} I_{mW}^{i,j} \quad (25)$$

where $I_{mW}^{i,j}$ represents the interference in mWs to the FN of the main link i occurred by a wireless transmission of the UE at link j (i.e. $j \in \mathcal{J}: j \neq i$), and $\mathcal{J}$ is the set of all possible links. Moreover, the individual interference resulting from the transmission on link j can be determined by transforming its value from the dBm scale into mW scale by:

$$I_{mW}^{i} = 10^{\left(\frac{I_{dBm}^{i,j}}{10}\right)} \quad (26)$$

in which the interference in dBm scale due to a transmission on a single path j is given by:

$$I_{dBm}^{i,j} = P_{dBm}^{j} + G_{dBi}^{j,Tx}(\varphi^{*}, \vartheta^{*}) + G_{dBi}^{i,Rx} - \mathcal{L}(d_{i,j}) \quad (27)$$

where P_{dBm}^{j} denotes the radiated power by the UE on wireless link j in dBm scale, $G_{dBi}^{i,Rx}$ stands for the receive antenna gain of the FN at the main link i (note that we assumed that $G_{dBi}^{i,Rx} =$

Table 2
Parameters of 28 GHz and 38 GHz mmWaves Close-In path loss.

Frequency	Dual-slope			Single-slope	
	β_1	β_2	d_{th} [m]	β_{LOS}	β_{NLOS}
28 GHz	2.2	2.7	129	2.1	2.6
38 GHz	2.9	4.4	205	1.9	2.7

0), $G_{dBi}^{j,Tx}(\varphi^*, \vartheta^*)$ represents the transmit antenna gain of the UE on link j to the FN of link i, wherein by assuming there is no misalignment in the system in such way that the UE at link j is aligned with its associated FN in the same link. Hence, φ^* and ϑ^* are used to express the azimuth and elevation angular differences between the UE of link j and the FN in link i, respectively. And $\mathcal{L}(d_{i,j})$ is the attenuation as a function of $d_{i,j}$ which is the 3D separation distance between the UE of link j and the FN of link i. Herein, $\mathcal{L}(d_{i,j})$ can be expressed as a summation of the path loss attenuation and the oxygen attenuation as a function of $d_{i,j}$ as explained before in the previous section.

5.3. Background noise calculations

The background noise n_{mW} can be calculated by converting it from the dBm scale into the mW scale as follows:

$$n_{mW} = 10^{\left(\frac{n_{dBm}}{10}\right)} \tag{28}$$

where the background noise in dBm scale n_{dBm} can be evaluated as follows:

$$n_{dBm} = k_B T_e + 10\log_{10}(BW) + NF + L_{IMP} \tag{29}$$

wherein the noise spectral density $k_B T_e = -174$ dBm/Hz [30], BW is the bandwidth of the studied frequency (i.e. 1 GHz [50]), the noise figure NF is 5 dB, and the value of the implementation loss L_{IMP} is assumed to be 10 dB [48].

6. Simulation results

In this paper, intensive numerical simulations are carried out on a hyperconnected F-RAN for a four different network deployment scenarios over a circular area of radius $r = 500$ m, for all scenarios the UEs are scattered over the entire area according to a homogeneous PPP. A typical UE is assumed to be located at the origin. In addition, we consider four different deployment models of the FNs including: PPP, GPP, square grid and UDN model. We set the FNs heights to 6 m and the and UEs heights to 1.5 m. The parameters for 28 GHz and 38 GHz mmWaves Close-In model are listed in Table 2, which are based on a real experimental measurements carried out at the campus of The University of Texas in USA and Aalborg University in Denmark for outdoor urban macro-cellular scenarios [25].

In this performance study the interference impacts from the randomly scattered UEs over the deployment area on the main wireless uplink between the typical UE and its associated FN is calculated in terms of SINR. We consider a location-based association scheme in which we assumed that the UEs are perfectly aligned with their associated FNs. The randomness of the antenna radiation pattern's azimuth and elevation angles directions of the randomly scattered interfering UEs is considered in the study. For each network deployment scenario, we studied the impacts of the number of interfering UEs for a fixed FN density, also the impacts of number of deployed FN for a fixed UE densities are studied too. We obtained the simulation results by averaging after performing 100 Monte-Carlo iterations.

Figs. 4 to 6 illustrate the achievable channel capacity of 28 GHz mmWave hyperconnected F-RAN for different parameters and deployment models. We can observe that the achievable capacities using the dual-slope model is higher than NLOS single-slope case, whereas it is slightly lower than LOS single-slope case. This mainly because the near-field PLE β_1 of the dual-slope model is quite lower than the NLOS PLE, whereas it is slightly higher than LOS PLE as Table 2 depicts. The channel capacity of 28 GHz mmWave hyperconnected F-RAN versus UE density for PPP, GPP and square grid network deployment scenarios at fixed FN density of 66 FNs/km^2 is plotted in Fig. 4. As shown in Fig. 4a, when the FNs are deployed according PPP model the maximum achievable capacity using Shannon's formula for LOS and NLOS single-slope models are about 4.8 Gbps and 2.6 Gbps, respectively. Whereas the maximum estimated capacity using the dual-slope model is around 4.4 Gbps which is 0.4 Gbps (about 10%) less than its value using LOS single-slope model. The capacity values drop to the half when the density of interfering UEs is only 50 UEs/km^2, whereas it is about one fourth its maximum values when the density of interfering UE increases to 100 UEs/km^2. Moreover, the achievable capacities become below 1 Gbps with 150 interfering UEs/km^2 and their values keep decreasing linearly after that to reach about 0.3 Gbps at 500 interfering UEs/km^2. As Figs. 4b and 4c depict the channel capacity versus the user density for GPP and square grid deployed FN exhibits the same behavior as PPP case, where the upper limits of the capacity for GPP scenario are about 5.2 Gbps using LOS single-slope model, 2.8 Gbps using NLOS single-slope model and 4.8 Gbps for dual-slope model, these values drop to the half when the density of interfering UEs is near 60 UEs/km^2, become below 1 Gbps at the density of 175 UEs/km^2 with a tendency for a linear decrease after that to be around 0.3 Gbps at the maximum interfering UE density of 500 UEs/km^2. Whereas the values of the maximum capacities for square grid network are near 6 Gbps, 5.4 Gbps, and 3.6 Gbps for LOS single-slope, NLOS single-slope and dual-slope models, respectively. At an interfering UE density of about 100 UEs/km^2 the capacity become almost the half of its maximum values and become less than 1 Gbps when the interfering UE density is more than 250 UEs/km^2. At a density of 500 interfering UEs/km^2 the square grid model achieves a capacity of 0.4 Gbps. It is quite obvious that the GPP network model achieves higher capacities than PPP model this mainly due to the repulsive nature of the GPP which results in more regularity for the FN deployment, this means that the length of the main link between the typical UE and its associated FN is stochastically less than the PPP scenario, equivalently, this results in a stronger received signal power of the main link. The impact of the regularity of FN deployment on the network performance is more obvious in square grid network model as it achieved much higher capacities than PPP and GPP models due the regular placement of FNs. We also observed that when the interfering UE density is high (i.e. greater than 150 UEs/km^2) the massive accumulation of the interference component dominates and degrades the performance, in such way the differences between the capacities of the considered path loss models are not noticeable (i.e. in terms of 10s Mbps). This proves that the interference impacts may not be ignorable for the massive accumulation of mmWave interference component even when the propagated desired signal experiences low PLEs.

Fig. 5 plots the channel capacity of 28 GHz F-RAN versus the FN density when the interfering user density is 200 UEs/km^2. This figure reveals a sharp performance improvement as the density of FN increases, which is due to two factors; First, the increase in the FN density results in a shorter length of the main link, hence a stronger received signal, this is also the reason behind the higher performance of the higher degree of regular FN deployment in this case too. Second, as the density of FNs increases a larger number of the UEs in the vicinity of the main FN that associated with it and their antennas aligned to it will be associated with

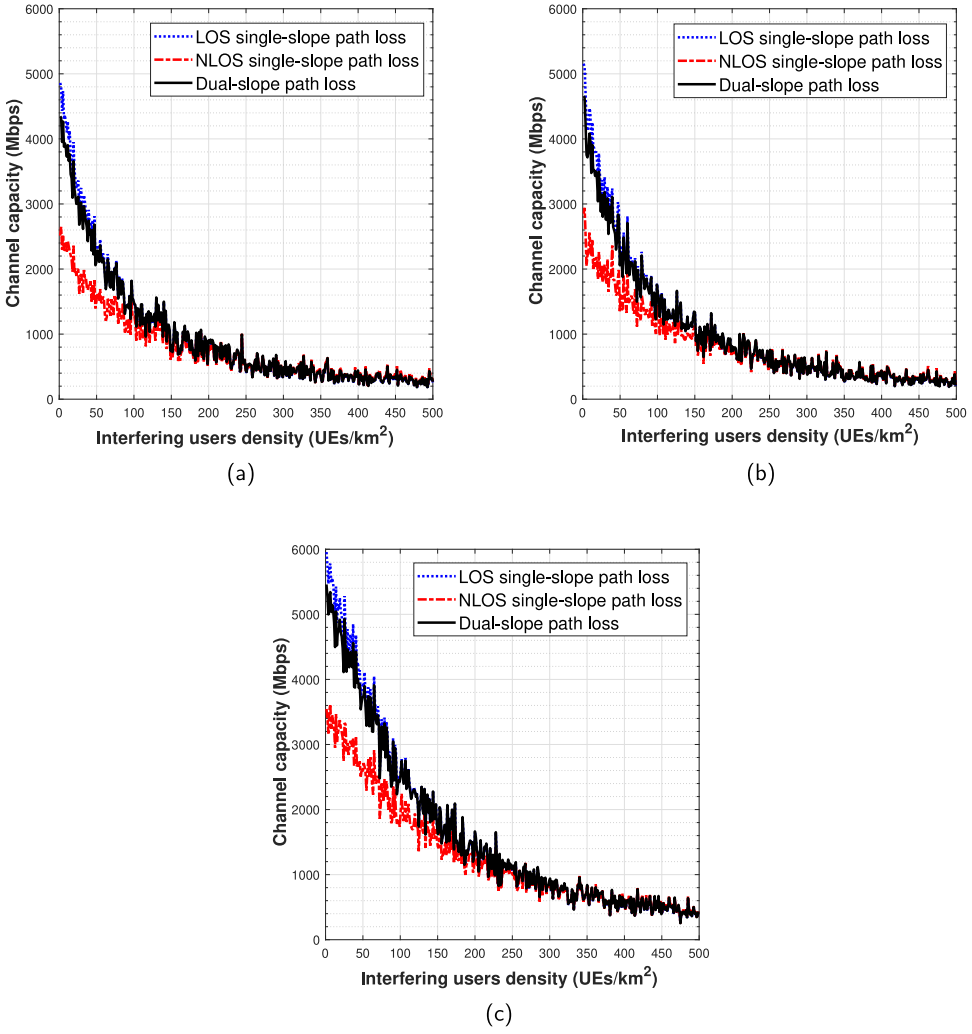

Fig. 4. Channel capacity of 28 GHz mmWave F-RAN versus UE density at a FN density of $\lambda_{FN} = 66$ FNs/km^2, (a) PPP network model, (b) GPP network model, (c) square grid network model.

other FNs that are closer to their locations, consequently their antennas will be aligned with their new associated FNs, which in turn results in angular differences that reduce the interfering UEs transmit antenna gains $G_{dBi}^{j,Tx}(\varphi^*, \vartheta^*)$ and hence the interference signals strength. It is also observed that the gaps in the performance between the path loss models increase with the increase in the FN density and degree of regularity, i.e. Fig. 5c shows larger gaps than Figs. 5a and 5b, which are become more obvious and larger when the FN density increases beyond 200 FNs/km^2, which is due to the lower accumulated interference with increase in the FN density and degree of regularity.

Yet, the aforementioned factors are the reasons of the vast performance improvement shown in Fig. 6 of UDN model wherein $\lambda_{FN} \geq 10^3$ FNs/km^2. Fig. 6a reports a tendency to a moderate linear decrease in the capacity with the increase in the density of the interfering UEs, where UDN model could achieve capacities over 4 Gbps at a high density of interfering UEs of 500 UEs/km^2. The figure further reveals a reduction in the gap between the performance using LOS single-slope and dual-slope models as the density of the interfering UEs increases to achieve almost the same performance after a density of 250 UEs/km^2. This phenomenon is also observed in Fig. 4 and can be explained by the fact that as the density of interfering UEs increases a larger number of interferers will reside at locations that have a separation distances from the main FN greater than the threshold distance of dual-slope model, hence when dual-slope model is used the interference signals from these UEs will experience a higher PLE than single-slope model, which in turn results in a lower accumulated interference signal that compensate the lower received signal of the main link. Fig. 6b illustrates the capacity improvement gained in UDN scenario as the density of FNs increases. A significant increasing trend is observed when the FN density is less than 2.5×10^3 FNs/km^2, where the capacity using LOS single-slope model increased from about 6 Gbps at 10^3 FNs/km^2 to about 9 GHz at 2.5×10^3 FNs/km^2. The gap in the performance using dual-slope model and LOS single-slope model is only in the range of 300 Mbps.

The performance of 38 GHz hyperconnected F-RAN is illustrated in Figs. 7 to 9. It is observed that the achievable capacity using dual-slope model is lower than the capacities of both LOS and NLOS single-slope models. This is due to the higher near-flied PLE β_1 of the dual-slope model compared with both LOS and NLOS single-slope models as shown in Table 2. In Fig. 7, we plot the channel capacity of 38 GHz F-RAN versus the density of interfering users for at FN density of 66 FNs/km^2 for PPP, GPP and square grid network models. Herein, the degree of regularity of FN deployment has an impact on the performance, where the achieved capacities by GPP model are higher than PPP model,

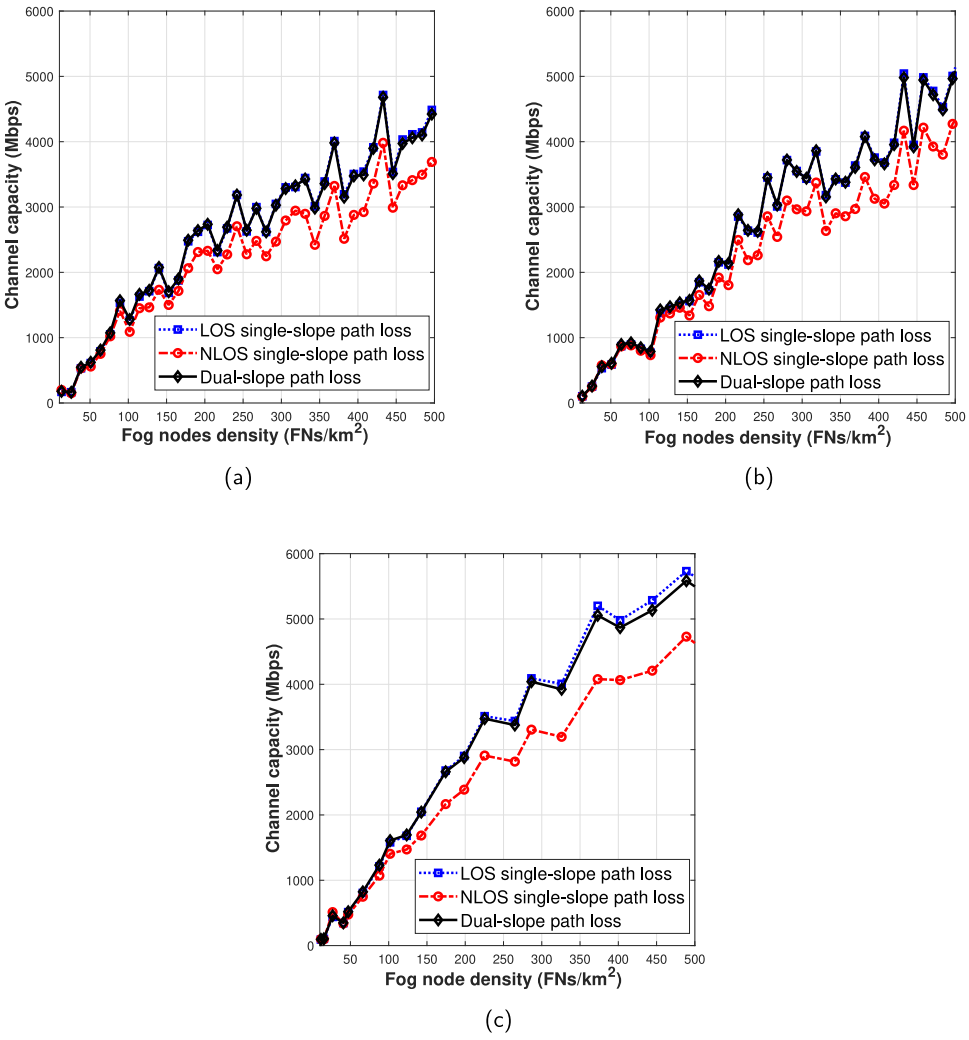

Fig. 5. Channel capacity of 28 GHz mmWave F-RAN versus FN density at an interfering user density of $\lambda_u = 200$ UEs/km^2, (a) PPP network model, (b) GPP network model, (c) square grid network model.

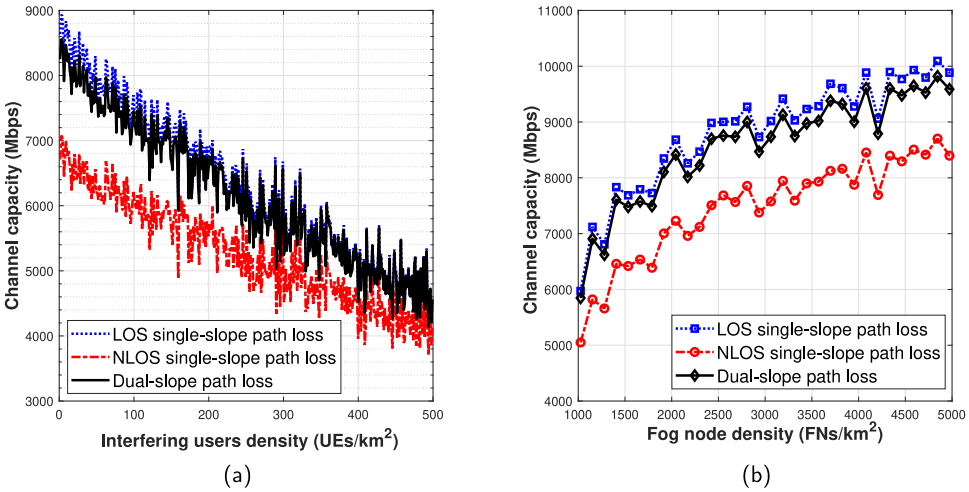

Fig. 6. Performance of 28 GHz mmWave F-RAN UDN model. (a) channel capacity versus interfering user density ($\lambda_{FN} = 10^3$ FNs/km^2), (b) channel capacity versus FN density ($\lambda_u = 200$ UEs/km^2).

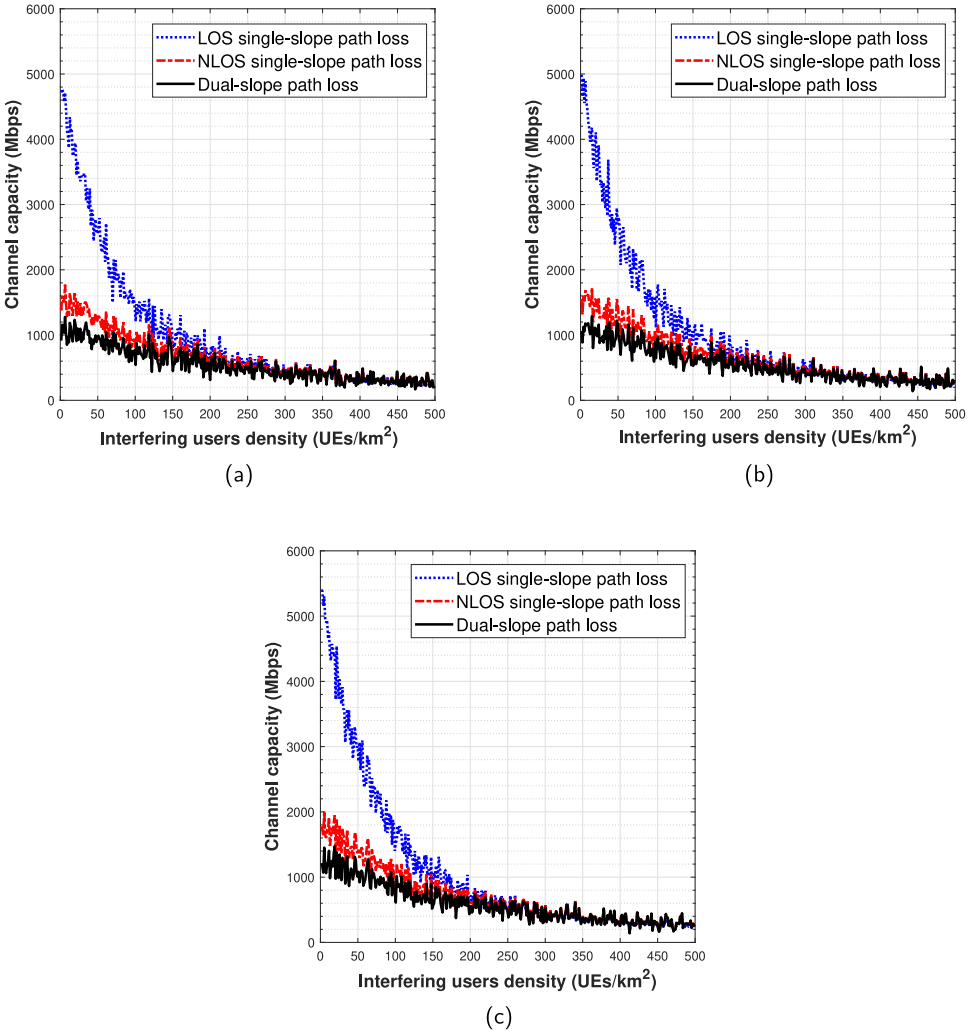

Fig. 7. Channel capacity of 38 GHz mmWave F-RAN versus UE density at a FN density of $\lambda_{FN} = 66$ FNs/km^2, (a) PPP network model, (b) GPP network model, (c) square grid network model.

but also lower than square gird network model which has the higher degree of regularity. Even though, the PLE of LOS single-slope path loss for of 38 GHz mmWave is less than 28 GHz case, 38 GHz LOS single-slope shows a lower performance, this due to the higher free space path loss and oxygen attenuation at 38 GHz. However, 38 GHz mmWave F-RANs show a high vulnerability towards massive accumulation of mmWave interference components where the capacity dropped dramatically below 1 Gbps as the interfering UE density increases to 150 UEs/km^2 for all the considered path loss and network models in this graph. The vulnerability towards the aggregated interference is more obvious when the interfering UE density is higher than 200 UEs/km^2, where the differences between the capacities of the considered path loss models tend to be not observable as the interfering UE density increases.

Fig. 8 compares the performance improvement gained by increasing the density of FNs for 38 GHz mmWave F-RAN PPP, GPP, and square grid FN deployment models when $\lambda_u = 200$ UEs/km^2. A dramatic performance improvement is observed when the density of FN increases as in 28 GHz case. Though, 38 GHz mmWave dual-slope model has a significantly high PLEs, it could achieve a desirable performance improvement as the FN density increases.

The performance of 38 GHz mmWave UDN F-RAN is illustrated in Fig. 9 at a FN density of 10^3 FNs/km^2. The observed performance in Fig. 9a shows a moderate decreasing trend as the interfering user density increases. At a high density of interfering users of 500 UEs/km^2 the average achievable capacities were above 2 Gbps for all the considered path loss models. In Fig. 9b, at an interfering user density of 200 UEs/km^2 a substantial increasing trend is observed. On average, the dual-slope model could achieve about 50% performance improvement by increasing the FN density from 10^3 FNs/km^2 to 2.5×10^3 FNs/km^2.

7. Limitations and future work

The major goal of this study was to examine the achievable capacities of wireless 28 GHz and 38 GHz mmWave F-RANs. The study was performed using dual-slope path loss models that based on real experimental campaigns for outdoor urban macro-cellular environment. The small number of data points of 38 GHz frequency band measurement campaign [25] led to higher PLEs of dual-slope model compared with LOS and NLOS single-slope models. Owing to this, the results using 38 GHz dual-slope model can serve as worst case scenario. Therefore, we suggest that more measurements need to be conducted to achieve more reliable multi-slope path loss models for 38 GHz mmWave frequency band. As far as the authors know, the multi-slope modeling of the

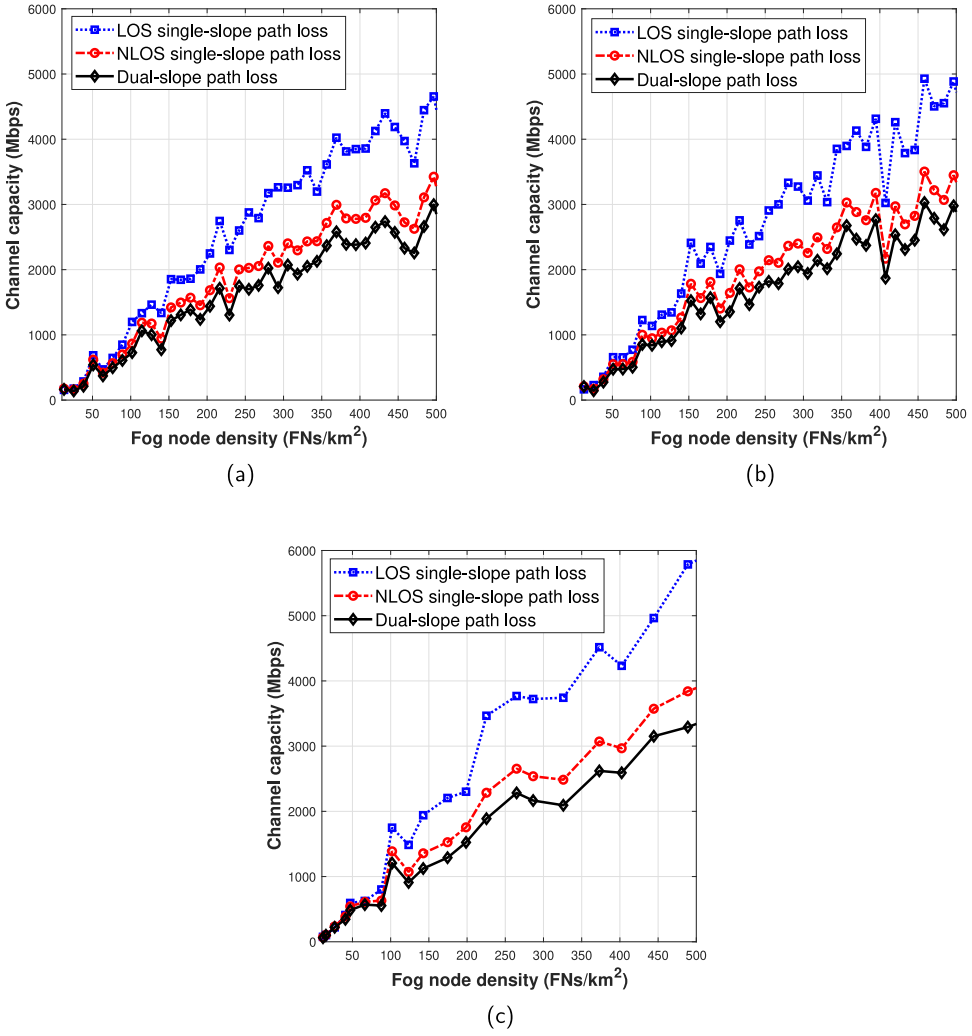

Fig. 8. Channel capacity of 38 GHz mmWave F-RAN versus FN density at an interfering user density of $\lambda_u = 200$ UEs/km^2, (a) PPP network model, (b) GPP network model, (c) square grid network model.

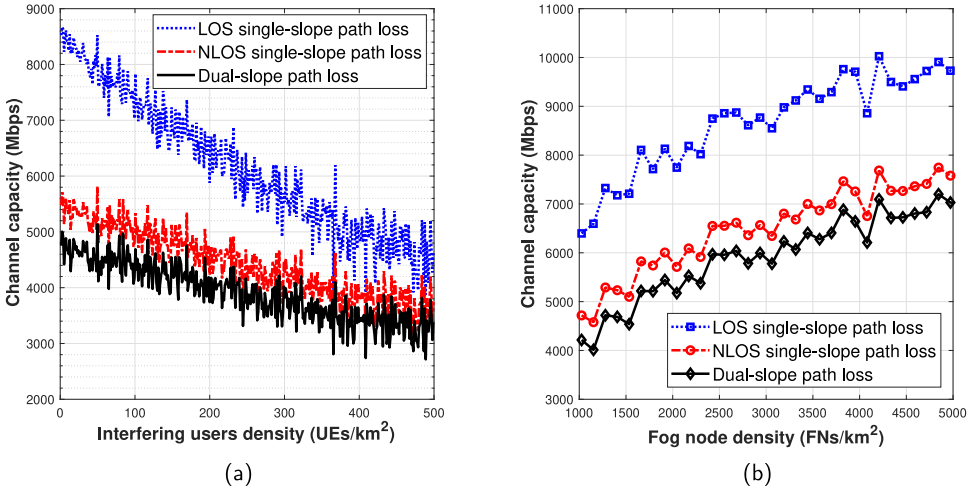

Fig. 9. Performance of 38 GHz mmWave F-RAN UDN model. (a) channel capacity versus interfering user density ($\lambda_{FN} = 10^3$ FNs/km^2), (b) channel capacity versus FN density ($\lambda_u = 200$ UEs/km^2).

path loss for other mmWave bands such as 60 GHz and 73 GHz bands is not explored and it is an open research field.

As a future study, we will conduct a similar feasibility study for 60 GHz and 73 GHz mmWave frequencies that are candidate frequencies for 5G. Additionally, the indoor environment will be studied. Besides, considering other repulsive FN deployment models. Furthermore, the mobility of both end users and FNs is of our interest. Lastly, the impact of the antenna radiation pattern will be examined by considering another directional antenna radiation patterns.

8. Conclusions

This paper estimates and analyzes the wireless interference impacts on the 28 GHz and 38 GHz mmWaves uplink transmissions of a hyperconnected F-RAN systems. In this performance study, the gain of the steerable antenna radiation patterns is formulated using a Gaussian mainlobe profile. Intensive SINR-based numerical performance simulations were carried out for PPP, GPP, square grid and UDN network deployment models. The obtained results compare the achievable channel capacity using dual-slope model with LOS and NLOS single-slope models. The results showed that massive accumulation of the interference components can severely impact the performance of mmWave F-RAN systems when the density of FN is low. However, as the density of FNs increases a significant performance improvement is observed for both 28 GHz and 38 GHz mmWaves. We also observe that FN deployment strategy with higher degree of regularity performs better, hence GPP deployment model due to its repulsive nature and therefore the higher degree of regularity could achieve a performance higher than PPP, but also it performs worse than square grid model the most regular deployment model. The results also showed that UDN model is less prone to the interference impacts owing to the shorter propagated distances and hence the lower attenuation, and also due to the lower interference signals strength because of the lower interfering UE transmit antenna gains due to the higher probability of angular differences between those UEs and the main FN. Lastly, the simulation results validate the feasibility of using 28 GHz and 38 GHz mmWaves in F-RANs when the density of interfering user is less than 150 UEs/km^2 where channel capacities higher than 1 Gpbs are achieved for all FN deployment models investigated in this paper.

CRediT authorship contribution statement

Alaa Bani-Bakr: Conceptualization, Methodology, Software, Formal analysis, Investigation, Data curation, Writing - original draft, Writing - review & editing, Visualization. **Kaharudin Dimyati:** Conceptualization, Methodology, Validation, Resources, Writing - review & editing, Visualization, Supervision, Project administration, Funding acquisition. **MHD Nour Hindia:** Conceptualization, Methodology, Validation, Formal analysis, Investigation, Resources, Data curation, Writing - original Draft, Writing - review & editing, Visualization, Supervision, Project administration, Funding acquisition. **Wei Ru Wong:** Formal analysis, Investigation, Data curation. **Muhammad Ali Imran:** Validation, Visualization.

Declaration of competing interest

The authors declare that they have no known competing financial interests or personal relationships that could have appeared to influence the work reported in this paper.

Acknowledgment

This work was partially supported by Engineering and Physical Sciences Research Council (EPSRC), United Kingdom grant No. [EP/P028764/1] [UM IF035-2017].

References

[1] Ericsson, Ericsson Mobility Report, Ericsson, Stockholm, Sweden, 2018.
[2] L. Chettri, R. Bera, A comprehensive survey on Internet of Things (IoT) toward 5G wireless systems, IEEE Internet Things J. 7 (1) (2020) 16–32.
[3] M. Aazam, S. Zeadally, K.A. Harras, Offloading in fog computing for IoT: Review, enabling technologies, and research opportunities, Future Gener. Comput. Syst. 87 (2018) 278–289.
[4] C. Perera, Y. Qin, J.C. Estrella, S. Reiff-Marganiec, A.V. Vasilakos, Fog computing for sustainable smart cities: A survey, ACM Comput. Surv. 50 (3) (2017) 32:1–32:43.
[5] F.A. Kraemer, A.E. Braten, N. Tamkittikhun, D. Palma, Fog computing in healthcare–A review and discussion, IEEE Access 5 (2017) 9206–9222.
[6] P. Hu, S. Dhelim, H. Ning, T. Qiu, Survey on fog computing: Architecture, key technologies, applications and open issues, J. Netw. Comput. Appl. 98 (2017) 27–42.
[7] M. Goudarzi, H. Wu, M.S. Palaniswami, R. Buyya, An application placement technique for concurrent IoT applications in edge and fog computing environments, IEEE Trans. Mob. Comput. (2020) 1.
[8] B. Omoniwa, R. Hussain, M.A. Javed, S.H. Bouk, S.A. Malik, Fog/edge computing-based IoT (FECIoT): Architecture, applications, and research issues, IEEE Internet Things J. 6 (3) (2019) 4118–4149.
[9] M. Anawar, S. Wang, M. Zia, A. Khan Jadoon, U. Akram, S.S. Raza, Fog computing: An overview of big IoT data analytics, Wirel. Commun. Mob. Comput. 2018 (2018) 1–22.
[10] E. Marín-Tordera, X. Masip-Bruin, J. García-Almiñana, A. Jukan, G.-J. Ren, J. Zhu, Do we all really know what a fog node is? Current trends towards an open definition, Comput. Commun. 109 (2017) 117–130.
[11] D. Ma, G. Lan, M. Hassan, W. Hu, S.K. Das, Sensing, computing, and communications for energy harvesting IoTs: A survey, IEEE Commun. Surv. Tutor. (2019) 1.
[12] V. Prokhorenko, M. Ali Babar, Architectural resilience in cloud, fog and edge systems: A survey, IEEE Access 8 (2020) 28078–28095.
[13] C.C. Byers, Architectural imperatives for fog computing: Use cases, requirements, and architectural techniques for fog-enabled IoT networks, IEEE Commun. Mag. 55 (8) (2017) 14–20.
[14] R.K. Naha, S. Garg, D. Georgakopoulos, P.P. Jayaraman, L. Gao, Y. Xiang, R. Ranjan, Fog computing: Survey of trends, architectures, requirements, and research directions, IEEE Access 6 (2018) 47980–48009.
[15] C. Mouradian, D. Naboulsi, S. Yangui, R.H. Glitho, M.J. Morrow, P.A. Polakos, A comprehensive survey on fog computing: State-of-the-art and research challenges, IEEE Commun. Surv. Tutor. 20 (1) (2018) 416–464.
[16] A. Osseiran, F. Boccardi, V. Braun, K. Kusume, P. Marsch, M. Maternia, O. Queseth, M. Schellmann, H. Schotten, H. Taoka, H. Tullberg, M.A. Uusitalo, B. Timus, M. Fallgren, Scenarios for 5g mobile and wireless communications: the vision of the METIS project, IEEE Commun. Mag. 52 (5) (2014) 26–35.
[17] M. Xiao, S. Mumtaz, Y. Huang, L. Dai, Y. Li, M. Matthaiou, G.K. Karagiannidis, E. Björnson, K. Yang, C. I, A. Ghosh, Millimeter wave communications for future mobile networks, IEEE J. Sel. Areas Commun. 35 (9) (2017) 1909–1935.
[18] NR; Base Station (BS) Radio Transmission and Reception (Release 16), Technical Report TS 38.104, 3GPP, 2019.
[19] Federal Communications Commission, Spectrum frontiers report and order and further notice of proposed rulemaking: FCC16- 89, 2016, https://docs.fcc.gov/public/attachments/FCC-16-89A1.pdf.
[20] W. Hong, Z.H. Jiang, C. Yu, D. Hou, H. Wang, C. Guo, Y. Hu, L. Kuai, Y. Yu, Z. Jiang, Z. Chen, J. Chen, Z. Yu, J. Zhai, N. Zhang, L. Tian, F. Wu, G. Yang, Z.C. Hao, J.Y. Zhou, The role of millimeter-wave technologies in 5g/6g wireless communications, IEEE J. Microw. 1 (1) (2021) 101–122.
[21] S.A. Busari, K.M.S. Huq, S. Mumtaz, L. Dai, J. Rodriguez, Millimeter-wave massive MIMO communication for future wireless systems: A survey, IEEE Commun. Surv. Tutor. 20 (2) (2018) 836–869.
[22] I.A. Hemadeh, K. Satyanarayana, M. El-Hajjar, L. Hanzo, Millimeter-wave communications: Physical channel models, design considerations, antenna constructions, and link-budget, IEEE Commun. Surv. Tutor. 20 (2) (2018) 870–913.
[23] K. Shehzad, N.M. Khan, J. Ahmed, Impact of frequency reuse and flexible cell association on the performance of dense heterogeneous cellular networks using dual-slope path loss model, IEEE Access 7 (2019) 166214–166234.

[24] H. Munir, H. Pervaiz, S.A. Hassan, L. Musavian, Q. Ni, M.A. Imran, R. Tafazolli, Computationally intelligent techniques for resource management in mmwave small cell networks, IEEE Wirel. Commun. 25 (4) (2018) 32–39.
[25] S. Sun, T.A. Thomas, T.S. Rappaport, H. Nguyen, I.Z. Kovacs, I. Rodriguez, Path loss, shadow fading, and line-of-sight probability models for 5g urban macro-cellular scenarios, in: 2015 IEEE Globecom Workshops (GC Wkshps), 2015, pp. 1–7.
[26] N. Garg, S. Singh, J. Andrews, Impact of dual slope path loss on user association in hetnets, in: 2015 IEEE Globecom Workshops (GC Wkshps), 2015, pp. 1–6.
[27] S.Q. Gilani, S.A. Hassan, H. Pervaiz, S.H. Ahmed, Performance analysis of flexible duplexing-enabled heterogeneous networks exploiting multi slope path loss models, in: 2019 International Conference on Computing, Networking and Communications (ICNC), 2019, pp. 724–728.
[28] S. Singh, R. Mudumbai, U. Madhow, Interference analysis for highly directional 60-GHz mesh networks: The case for rethinking medium access control, IEEE/ACM Trans. Netw. 19 (5) (2011) 1513–1527.
[29] J. Kim, J.-K. Kim, Achievable rate estimation of IEEE 802.11ad visual big-data uplink access in cloud-enabled surveillance applications, PLoS One 11 (12) (2016).
[30] J. Kim, W. Lee, Feasibility study of 60 GHz millimeter-wave technologies for hyperconnected fog computing applications, IEEE Internet Things J. 4 (5) (2017) 1165–1173.
[31] J. Kim, E. Ryu, Quality of video streaming in 38 GHz millimetre-wave heterogeneous cellular networks, Electron. Lett. 50 (21) (2014) 1526–1528.
[32] B. Błaszczyszyn, M. Haenggi, P. Keeler, S. Mukherjee, Stochastic Geometry Analysis of Cellular Networks, Cambridge University Press, 2018.
[33] N. Miyoshi, T. Shirai, A cellular network model with ginibre configured base stations, Adv. Appl. Probab. 46 (2014) 832–845.
[34] F. Qamar, K. Dimyati, M.N. Hindia, K.A. Noordin, I.S. Amiri, A stochastically geometrical Poisson point process approach for the future 5G D2D enabled cooperative cellular network, IEEE Access 7 (2019) 60465–60485.
[35] J.G. Andrews, F. Baccelli, R.K. Ganti, A tractable approach to coverage and rate in cellular networks, IEEE Trans. Commun. 59 (11) (2011) 3122–3134.
[36] N. Miyoshi, T. Shirai, Spatial modeling and analysis of cellular networks using the ginibre point process: A tutorial, IEICE Trans. Commun. E99.B (2016).
[37] C.A.N. Biscio, F. Lavancier, Quantifying repulsiveness of determinantal point processes, Bernoulli 22 (4) (2016) 2001–2028.
[38] N. Deng, W. Zhou, M. Haenggi, The ginibre point process as a model for wireless networks with repulsion, IEEE Trans. Wireless Commun. 14 (1) (2015) 107–121.
[39] D. Ramasamy, R. Ganti, U. Madhow, On the capacity of picocellular networks, in: 2013 IEEE International Symposium on Information Theory, 2013, pp. 241–245.
[40] K.A. Shah, D.C. Jinwala, Privacy preserving, verifiable and resilient data aggregation in grid-based networks, Comput. J. 61 (4) (2018) 614–628.
[41] M.N. Hindia, F. Qamar, T. Abbas, K. Dimyati, M.S.A. Talip, I.S. Amiri, Interference cancelation for high-density fifth-generation relaying network using stochastic geometrical approach, Int. J. Distrib. Sens. Netw. 15 (7) (2019) 1550147719855879.
[42] S.M.A. Zaidi, M. Manalastas, H. Farooq, A. Imran, Mobility management in emerging ultra-dense cellular networks: A survey, outlook, and future research directions, IEEE Access (2020) 1.
[43] M. Kamel, W. Hamouda, A. Youssef, Ultra-dense networks: A survey, IEEE Commun. Surv. Tutor. 18 (4) (2016) 2522–2545.
[44] M. Haenggi, A dense debate, 2020, https://stogblog.net/2020/12/04/a-dense-debate/.
[45] Y. Zhong, G. Mao, X. Ge, F.C. Zheng, Spatio-temporal modeling for massive and sporadic access, IEEE J. Sel. Areas Commun. 39 (3) (2021) 638–651.
[46] M.J. Feuerstein, K.L. Blackard, T.S. Rappaport, S.Y. Seidel, H.H. Xia, Path loss, delay spread, and outage models as functions of antenna height for microcellular system design, IEEE Trans. Veh. Technol. 43 (3) (1994) 487–498.
[47] X. Zhang, J.G. Andrews, Downlink cellular network analysis with multi-slope path loss models, IEEE Trans. Commun. 63 (5) (2015) 1881–1894.
[48] J. Kim, L. Xian, A.S. Sadri, Numerical simulation study for frequency sharing between micro-cellular systems and fixed service systems in millimeter-wave bands, IEEE Access 4 (2016) 9847–9859.
[49] ITU, Reference Radiation Patterns of Omnidirectional, Sectoral and Other Antennas for the Fixed and Mobile Services for use in Sharing Studies in the Frequency Range from 400 Mhz to About 70 Ghz, ITU, 2014.
[50] A. M Al-samman, T. Abd Rahman, M. Bin Azmi, M. Hindia, I. Khan, E. Hanafi, Statistical modelling and characterization of experimental mm-wave indoor channels for future 5G wireless communication networks, PLoS ONE 11 (2016).
[51] C. She, C. Yang, T.Q.S. Quek, Cross-layer optimization for ultra-reliable and low-latency radio access networks, IEEE Trans. Wireless Commun. 17 (1) (2018) 127–141.

Alaa Bani-Bakr received the B.Sc. and M.Sc. degrees in electrical/telecommunication engineering from Mutah University, Karak, Jordan, in 2002 and 2007, respectively. He is currently pursuing the Ph.D. degree with the University of Malaya, Kuala Lumpur, Malaysia. He was a Lecturer at the Department of Electrical Engineering, Al-Baha University, Saudi Arabia, from 2010 to 2012. His research interests are fog computing, stochastic analysis, and mmWave communication systems.

Kaharudin Dimyati graduated from the University of Malaya, Malaysia, in 1992. He received the Ph.D. degree from the University of Wales Swansea, U.K., in 1996. He is currently a Professor at the Department of Electrical Engineering, Faculty of Engineering, University of Malaya. Since joining the university, he is actively involved in teaching, postgraduate supervision, research, and also administration. To date, he has supervised 15 Ph.D. students and 32 master by research students. He has published over 100 journal articles. He is a member of IET and IEICE. He is a Professional Engineer and a Chartered Engineer.

Mhd Nour Hindia received the Ph.D. degree from the Faculty of Engineering in Telecommunication, University of Malaya, Kuala Lumpur, Malaysia, in 2015. He is currently involved with research in the field of wireless communications, especially in channel sounding, network planning, converge estimation, handover, scheduling, and quality of service enhancement for 5G networks. He is currently a Post-Doctoral Fellow from the Faculty of Engineering in Telecommunication, University of Malaya. Besides that, he is involved with research with the Research Group in Modulation and Coding Scheme for Internet of Things for Future Network. He has authored or co-authored a number of science citation index journals and conference papers. Dr. Hindia has participated as a Reviewer and a committee member of a number of ISI journals and conferences.

Wei Ru Wong received the B.Eng. and Ph.D. degrees from the Department of Electrical Engineering, University of Malaya, Kuala Lumpur, Malaysia. After receiving the Ph.D. degree, she was a Postdoc with the Integrated Lightwave Research Group, University of Malaya. Her Ph.D. thesis involved the development of long-range surface plasmon based biosensor for dengue detection. She is currently a Senior Lecturer with the Department of Electrical Engineering, University of Malaya. Her work on dengue biosensor has received significant press coverage. Her research interests include the development of planar waveguides and optical fibers for sensing applications especially those implemented using surface plasmons.

Muhammad Ali Imran received the M.Sc. (Distinction) and Ph.D. degrees from Imperial College London, U.K., in 2002 and 2007, respectively. He is a Professor of wireless communication systems. He heads the Communications, Sensing and Imaging (CSI) research group, University of Glasgow, Glasgow, U.K., and is the Dean with the University of Glasgow, for the University of Electronic Science and Technology China programs. He is an Affiliate Professor with the University of Oklahoma, Norman, OK, USA, and a Visiting Professor with 5G Innovation Center, University of Surry, Guilford, U.K. He has filed 15 patents; has authored/co-authored more than 400 journal and conference publications; and has successfully supervised more than 40 postgraduate students at Doctoral level. His research interests include self-organized networks, wireless networked control systems, and the wireless sensor systems. Prof. Imran is a Fellow of the Institution of Engineering and Technology and a Senior Fellow of the Higher Education Academy (HEA).